Line Detection as an Inverse Problem: Application to Lung Ultrasound Imaging

Nantheera Anantrasirichai, *Member, IEEE*, Wesley Hayes, Marco Allinovi, David Bull, *Fellow, IEEE*, and Alin Achim, *Senior Member, IEEE*

Abstract—This paper presents a novel method for line restoration in speckle images. We address this as a sparse estimation problem using both convex and non-convex optimization techniques based on the Radon transform and sparsity regularization. This breaks into subproblems, which are solved using the alternating direction method of multipliers, thereby achieving line detection and deconvolution simultaneously. We include an additional deblurring step in the Radon domain via a total variation blind deconvolution to enhance line visualization and to improve line recognition. We evaluate our approach on a real clinical application: the identification of B-lines in lung ultrasound images. Thus, an automatic B-line identification method is proposed, using a simple local maxima technique in the Radon transform domain, associated with known clinical definitions of line artefacts. Using all initially detected lines as a starting point, our approach then differentiates between B-lines and other lines of no clinical significance, including Z-lines and A-lines. We evaluated our techniques using as ground truth lines identified visually by clinical experts. The proposed approach achieves the best B-line detection performance as measured by the F score when a non-convex ℓ_p regularization is employed for both line detection and deconvolution. The F scores as well as the receiver operating characteristic (ROC) curves show that the proposed approach outperforms the state-of-the-art methods with improvements in B-line detection performance of 54%, 40%, and 33% for $F_{0.5}$, F_1, and F_2, respectively, and of 24% based on ROC curve evaluations.

Index Terms—Line detection, deconvolution, image restoration, ultrasound, inverse problem, ADMM, sparsity regularisation.

I. INTRODUCTION

L INES and boundaries in medical images frequently represent important structures as they can discriminate tissue types, organs, and membranes. Although a number of image enhancement and segmentation methods have been proposed to help detect lines, none of these have considered line artefacts, which are more difficult to visualise, yet are still meaningful for clinical interpretation. One such clinical application is the detection of B-line artefacts in lung ultrasound images. The summation of these B-lines yields a score denoting the extent of extravascular fluid in the lungs [1]–[3]. Notwithstanding progress in dialysis techniques, volume overload and cardiopulmonary congestion remain a major problem in patients on hemodialysis and peritoneal dialysis.

Fluid status assessment is one of the challenging goals for the nephrologist in patients on dialysis, characterized by a profound impairment in the regulation of body fluid distribution. Various techniques have been employed to quantify fluid overload in patients with end stage kidney disease, and among them lung ultrasonography has attracted growing attention in recent years [4]. B-lines are imaging artefacts which result from subclinical transudate resulting in acoustic mismatch between the lung parenchyma and adjacent pleura. Moderate to severe lung congestion detected via quantification of B-lines using lung ultrasound is a strong predictor of intradialytic morbidity, death and cardiovascular events in adult dialysis patients [5], [6]. The technique has also shown potential as a superior predictor of fluid overload in infants and children on dialysis when compared to other measures [2], [3]. Clinical limitation when using lung ultrasound to quantify fluid overload is that quantification of B-lines may not accurately reflect generalised fluid overload in patients with conditions such as interstitial lung disease or severe cardiac disease. Moreover, the technique is operator dependent and requires specialist training [7]. This limits the application of lung ultrasound in the clinical setting, as only a small number of trained individuals can reliably detect B-lines. Hence, a small number of patients have access to lung ultrasound, and it is not routinely used in paediatric practice. Therefore, reliable image processing techniques that improve the visibility of lines and facilitate line detection in speckle images are essential. To the best of our knowledge, only two automatic approaches [8], [9] and one semi-automatic approach [10] have been proposed previously. The method in [8] employs angular features and thresholding (AFT). A B-line is detected in a particular image column if each feature exceeds a predefined threshold. The method in [9] uses alternate sequential filtering (ASF). A repeated sequential morphological opening and closing approach is applied to the mask until potential B-lines are separated. These methods are far from being sufficiently

reliable to be used in clinical settings. This is particularly true for paediatric ultrasound data due to the anatomical differences between children and adults.

For line detection, the Hough transform is the most popular algorithm due to its simplicity. The transform uses a parametric representation of a line: $r = x \cos(\theta) + y \sin(\theta)$, where r is the shortest distance between the origin and the line, and θ is an angle between the x axis and a vector perpendicular to the line [11]. Applying the Hough transform is however not straightforward in noisy images, particularly for multiplicative speckle noise, as often encountered in medical images, due to the multiple false peaks generated from collinear noisy edge points. Several techniques have been proposed to deal specifically with speckle noise [12], [13]. For example, the method in [14] employs an adaptive-weighted bilateral filtering (AWBF) to reduce speckle and preserve edge structure by computing local entropy. Some techniques have focused on line detection in noisy images [15], [16]. This includes the method introduced by Czerwinski *et al.* [17] that uses eight directional sticks as a rotating kernel transformation to enhance lines and curves in ultrasound images. A review of edge and line detection methods using different denoising filters can be found in [18]. These techniques generally require several predefined thresholds and parameters, and hence need tuning for use with data collected in different settings.

A Radon transform was employed to avoid the binary edge detection process in [19]. This is similar to the Hough transform but it directly operates on grayscale images [20]. Aggarwal and Karl [21] proposed one such line detection method based on the Radon transform and showed very promising results. However, when they applied their method to real images (e.g. aerial and SAR images), the grayscale images were converted to binary gradient images, which means that a predefined threshold is still required. Moreover, their method does not consider blur that generally occurs due to imperfect image acquisition, e.g. defocus, or machine limitations, such as low resolution and slow shutter speed.

In this paper, we propose a novel solution to an inverse problem for line detection in ultrasound images. This extends from our previous work [22], where lines in noisy ultrasound images were modelled via a Radon transform only and they were estimated using ℓ_1 regularisation. Here, we combine a Radon transform with the point spread function (PSF) of the ultrasound acquisition system in a single equation thereby achieving line detection and deconvolution simultaneously. This inverse problem is solved using the alternating direction method of multipliers (ADMM) [23], offering a fast convergence rate. We present solutions for various ℓ_p regularisations, where $p > 0$ (small p leads to sparsity). We subsequently show that the proposed method is suitable for B-line detection in lung ultrasound images. The method also detects Z-lines and A-lines in order to distinguish B-lines. Z-lines also appear as vertical lines, but are not caused by an increase in lung density so they must be discounted. The A-lines, which are reflections of the pleural lines, help separating B-lines and Z-lines. We specifically address images of children as these are technically challenging due to chest size and rib positions. These images are generally low-resolution and show obvious rib shadows causing images to be low contrast.

The novel contributions of this work are summarised as follows:

1) We propose an innovative way of detecting lines in speckle images by solving an inverse problem;
2) We address the issue of joint line detection and deconvolution, with the latter component being essential for the accuracy of the former;
3) We propose solutions to the above inverse problems based on both convex and non-convex optimisation approaches with fast rates of convergence;
4) We introduce an automatic robust approach to B-lines identification amongst various line artefacts present in lung ultrasound, which also include the pleural line, A-lines and Z-lines.

The remaining part of this paper is organised as follows. In Section II we describe lung ultrasound imaging and associated line artefacts. Then, the proposed line restoration via an inverse problem solving is presented in Section III. An enhanced method using an additional deblurring step is described in Section IV. The B-line identification method, which uses the set of previously restored lines, is presented in Section V. The performance of the proposed methods is evaluated on sets of both simulated and real ultrasound images in Section VI. Finally, Section VII presents the conclusions of the paper.

II. CHARACTERISATION OF LUNG ULTRASOUND IMAGES

A. Line Artefacts and Their Clinical Meaning

Lung ultrasound, is a non-invasive, easy-to-perform, radiation-free, fast, cheap and highly reliable technique, which is currently employed for objective monitoring of pulmonary congestion [24]. The technique requires ultrasound scanning of the anterior right and left chest, from the second to the fifth intercostal space, in multiple intercostal spaces [25]. The soft tissues of the chest wall and the aerated lung are separated by a pleural line, which is thin, hyperechoic and curvilinear.

Linear artefacts are thought to arise from ultrasound reverberations generated by the water-thickened interlobular septa and other subpleural structures [26]. These artefacts are referred to as B-lines. When the air content decreases and lung density increases due to the presence in the lung of transudate, the acoustic mismatch between the lung and the surrounding tissues is lowered, and the ultrasound beam can be partly reflected at deeper zones and repeatedly. This phenomenon creates discrete vertical hyperechoic reverberation artefacts (B-lines), that arise from the pleural line [27]. The presence of a few scattered B-lines can be a normal variant, found in healthy subjects, especially in the lower intercostal spaces. Multiple B-lines are considered sonographic sign of lung interstitial syndrome, and their number increases along with decreasing air content and increase in lung density [28]. Note that the B-lines are counted as one if they originate from the same point on the pleural line.

A-line artefacts are repetitive horizontal echoic lines with equidistant intervals, which are also equal to the distance
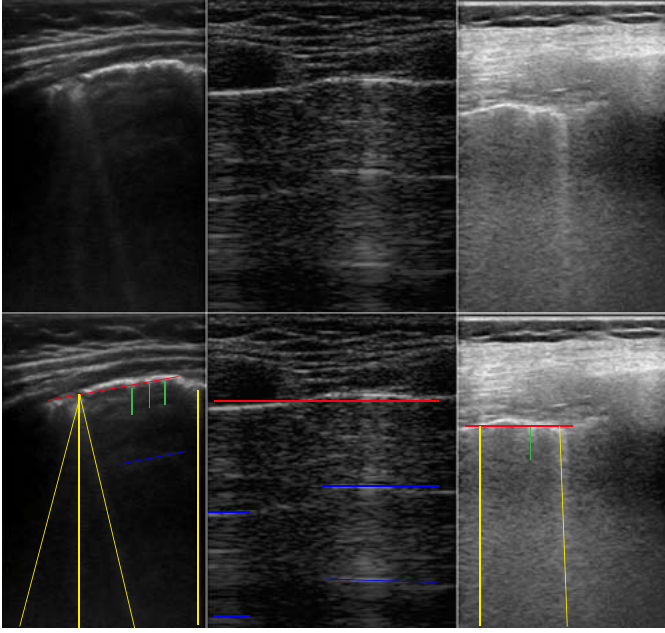
Fig. 1.   Line artefacts in lung ultrasound images. B-mode images (top row) and lines overlaid on them (bottom row). There are two, zero and two B-lines in the image on the left, middle and right, respectively. Red, yellow, blue and green lines represent the pleural lines, B-lines, A-lines and Z-lines, respectively.

between skin and pleural line [1]. The A-lines indicate sub-pleural air, which completely reflects the ultrasound beam. The length of an A-line can be roughly the same as the pleural line, but it can also be shorter, or even not visible because of sound beam attenuation through the lung medium. Finally, Z-lines are short vertical comet tail artefacts arising from the pleural line but not reaching the distal edge of the screen. They are found in normal persons as well as in those with an abnormal collection of air in the pleural space. They do not erase the A-lines and do not move with lung sliding. They are of no clinical significance, so they should not be confused with the B-lines. Fig. 1 shows various line artefacts in lung ultrasound images, occurring in different machine settings.

B. Line Artefact Model

The simplest way of modelling lines in noisy images is by

$$y = \mathcal{C}x + n, \tag{1}$$

where $y(i, j)$ is the observed noisy image ($h \times w$) in the two-dimensional Euclidean plane, $i \in (-\frac{h}{2}, \frac{h}{2}]$, $j \in (-\frac{w}{2}, \frac{w}{2}]$. $x(r, \theta)$ is the line represented by a distance r from the centre of y and a orientation θ from the the horizontal axis of the image, and n is noise. $\mathcal{C} = \mathcal{R}^{-1}$ is an inverse Radon transform. In its general form without noise, a Radon transform $\mathcal{R}$ is described in (2), where $\delta(\bullet)$ is a delta function. This is the integral of the image intensity over the hyperplane perpendicular to θ, and projected on to a radial line oriented at θ.

$$x(r, \theta) = \int_{\mathbb{R}^2} y(i, j)\delta(r - i\cos\theta - j\sin\theta)di\,dj. \tag{2}$$

An inverse Radon transform $\mathcal{C}$ can be obtained using the filtered backprojection algorithm [29]. It comprises a filtering part (with the filter $|v|$ in the Fourier domain) and a backprojection part, expressed in (3a) and (3b), respectively.

$$g(r, \theta) = \mathrm{IFT}_{v \to r}\left(|v|\, \mathrm{FT}_{r \to v}(x(r, \theta))\right), \tag{3a}$$

$$y(i, j) = \int_0^\pi \int_{\mathbb{R}} g(r, \theta)\delta(r - i\cos\theta - j\sin\theta)dr\,d\theta, \tag{3b}$$

where v is the radius in Fourier domain, $\mathrm{FT}_{r \to v}$ is a forward Fourier transform in the r to v direction, and $\mathrm{IFT}_{v \to r}$ is an inverse Fourier transform from v to r. To operate with an image, $\mathcal{R}$ and $\mathcal{C}$ are discrete and can be implemented as proposed in [30]. In this paper, we used MATLAB functions *radon* and *iradon* to construct $\mathcal{R}$ and $\mathcal{C}$, respectively [31]. An example of l ung ultrasound i mage and its Radon transform is shown in Fig. 2.

For ultrasound images in particular, the lines can be more precisely described using the model

$$y = \mathcal{H}\mathcal{C}x + n, \tag{4}$$

where $\mathcal{H}$ is a point spread function (PSF). The PSF of the ultrasound system is spatially variant, particularly in the axial direction of the ultrasound image. This spatial variation can be compensated during the image acquisition or post-processing, e.g. the time gain compensation (TGC) [32]. We therefore employ the spatially invariant PSF, which can simply be extended to the spatially variant case by applying overlapped partition techniques [33], [34].

III. PROPOSED LINE RESTORATION IN SPECKLE IMAGES

To detect B-lines in lung ultrasound images, two major steps are proposed: i) line restoration (Section III-A) using image regularisation based on the Radon transform, and ii) B-line identification (Section V-B), following the occurrence of line artefacts in the ultrasonic domain [35].

A. Optimisation Problem

Equation (4) poses an inverse problem for finding x, and can be seen as two separate subproblems which can be solved with two optimisation processes. The first step is to restore the image w from the blurred speckle image $y = \mathcal{H}w$ by solving

$$\hat{w} = \arg\min_w \{||y - \mathcal{H}w||_2^2 + \alpha ||w||_p^p\}, \tag{5}$$

where $p > 0$ is related to the shape of the statistical distribution of the ultrasound image. $p = 1$ and $p = 2$ are for the Laplacian model and Gaussian model, respectively. $p < 1$ determines a non-convex penalty function, which achieves the approximation of the ideal ℓ_0 case. The choice of p can be related to an SαS distribution characterising ultrasound images as shown in [36] and [37].

The second process is to estimate the lines in the Radon transform domain x from the image $w = \mathcal{C}x$, as shown in (6). Here we strictly employ $\ell_q, 0 < q \leq 1$ norm in the regulariser for enforcing sparsity as intuitively a collection of thin lines determine a sparse dataset.

$$\hat{x} = \arg\min_x \{||\hat{w} - \mathcal{C}x||_2^2 + \beta ||x||_q^q\}. \tag{6}$$

Solving two optimisation problems separately is computationally inefficient; therefore, we estimate x and w simultaneously by solving the following optimisation problem:

$$\hat{x} = \arg\min_{x}\{||y - \mathcal{H}\mathcal{C}x||_2^2 + \alpha||\mathcal{C}x||_p^p + \beta||x||_q^q\}. \quad (7)$$

If the step size for θ is large, e.g. $\Delta\theta > 1°$, a smoothness term $\gamma||\nabla\mathcal{C}x||_1$ should be included in (7) to suppress the quantisation noise, which is due to the discrete predefined range of orientations Θ [22].

B. Implementation

The alternating direction method of multipliers (ADMM) [23] is employed to solve the problem in (7). It is a variant of the augmented Lagrangian scheme that uses partial updates for the dual variables. It is easy to implement by splitting a large problem into a series of subproblems:

$$\text{minimize } f(u) + g(v)$$
$$\text{subject to } \mathcal{A}u - \mathcal{B}v = 0. \quad (8)$$

where

$$f(u) = ||y - \mathcal{H}u||_2^2, \quad u = w = \mathcal{C}x, \quad (9a)$$
$$g(v) = \alpha||w||_p^p + \beta||x||_q^q + \gamma||\nabla\mathcal{C}x||_1, \quad v = [w \ x]^T, \quad (9b)$$
$$\mathcal{A} = \begin{bmatrix} \mathcal{I} \\ \mathcal{I} \end{bmatrix}, \quad \mathcal{B} = \begin{bmatrix} \mathcal{I} & 0 \\ 0 & \mathcal{C} \end{bmatrix}. \quad (9c)$$

u^T indicates the transpose of u, and $\mathcal{I}$ is the identity matrix with the same size as y which is $N \times N$. Then, the augmented Lagrangian for (8) is

$$\mathcal{L}_\rho(u, v, z) = ||y - \mathcal{H}u||_2^2 + \alpha||w||_p^p + \beta||x||_q^q$$
$$+ \gamma||\nabla\mathcal{C}x||_1 + z^T(\mathcal{A}u - \mathcal{B}v) + \frac{\rho}{2}||\mathcal{A}u - \mathcal{B}v||_2^2, \quad (10)$$

where $z = [z_1 \ z_2]^T$ is the dual variable or Lagrange multiplier, $z_1 \in \mathbb{R}^{N \times N}$, $z_2 \in \mathbb{R}^{N \times N}$. $\rho > 0$ is a penalty parameter. To solve the case of non-convex problems, ρ is chosen to be large and bounded as suggested in [38]. The ADMM technique allows this problem to be solved approximately using the following three-step iterations.

$$u^{k+1} := \arg\min_{u} \mathcal{L}_\rho(u, v^k, z^k), \quad (11a)$$
$$v^{k+1} := \arg\min_{v} \mathcal{L}_\rho(u^{k+1}, v, z^k), \quad (11b)$$
$$z^{k+1} := z^k + \rho(\mathcal{A}u^{k+1} - \mathcal{B}v^{k+1}). \quad (11c)$$

where k is an internal iteration counter. As $v = [w \ x]^T$, the problem in (11b) can be divided into two subproblems to restore w^{k+1} and x^{k+1} independently. The algorithm stops with the convergence criterion $||x^{k+1} - x^k||/||x^k|| < \epsilon$, where ϵ is a very small number ($\epsilon = 10^{-3}$ in this paper). In the following, we describe the ADMM algorithm for solving (11).

1) Solving u^{k+1}: The problem in (11a) is a quadratic function about u, which can be solved as follows.

$$u^{k+1} = \arg\min_{u} ||y - \mathcal{H}u||_2^2 + (z^k)^T(\mathcal{A}u - \mathcal{B}v^k)$$
$$+ \frac{\rho}{2}||\mathcal{A}u - \mathcal{B}v^k||_2^2,$$
$$= (2\mathcal{H}^T\mathcal{H} + \rho\mathcal{A}^T\mathcal{A})^{-1}(2\mathcal{H}^T y + \rho\mathcal{A}^T\mathcal{B}v^k - (z^k)^T\mathcal{A}),$$
$$= (2\mathcal{H}^T\mathcal{H} + 2\rho\mathcal{I})^{-1}(2\mathcal{H}^T y + \rho w^k + \rho\mathcal{C}x^k$$
$$- z_1^k - z_2^k). \quad (12)$$

2) Solving w^{k+1} in v^{k+1}: We define $\lambda_1 = \alpha/\rho$ and add a constant offset $||z_1^k/\rho||_2^2$. Consequently, this is a form of proximal operator of $\lambda_1||w||_p^p$ and w^{k+1} can be computed depending on the value of p [39].

$$w^{k+1} = \arg\min_{w} \alpha||w||_p^p + (z_1^k)^T(u^{k+1} - w)$$
$$+ m\frac{\rho}{2}||u^{k+1} - w||_2^2,$$
$$= \arg\min_{w} \lambda_1||w||_p^p + \frac{1}{2}||u^{k+1} - w + \frac{z_1^k}{\rho}||_2^2,$$
$$= prox_{\lambda_1||.||_p^p}\left(u^{k+1} + \frac{z_1^k}{\rho}\right). \quad (13)$$

If $p = 1$ (ℓ_1 norm), the proximal operator is a soft thresholding described as

$$prox_{\lambda_1||.||_1}(a) = sign(a)\max(|a| - \lambda_1, 0). \quad (14)$$

If $p = 2$ (ℓ_2 norm or Euclidean norm), the proximal operator is a block soft thresholding described as

$$prox_{\lambda_1||.||_2}(a) = \max(1 - \lambda_1/||a||_2, 0)a. \quad (15)$$

If $0 < p < 1$ (non-convex ℓ_p norm), we employ an iterative algorithm of Generalized soft-thresholding (GST) [40], which proceeds as follows.

$$prox_{\tau_p||.||_p}(a) = T_p^{GST}(a, \lambda_1), \quad (16a)$$
$$T_p^{GST}(a, \lambda_1) = sign(a)\max(b^{t+1} - \tau_p(\lambda_1), 0), \quad (16b)$$
$$b^{t+1} = |a| - \lambda_1 p(b^t)^{p-1}, \quad (16c)$$
$$\tau_p(\lambda_1) = (2\lambda_1(1-p))^{\frac{1}{2-p}} + \lambda_1 p(2\lambda_1(1-p))^{\frac{p-1}{2-p}}, \quad (16d)$$

where t is an internal iteration counter for the process of (16c) and $b^0 = |a| = |u^{k+1} + \frac{z_1^k}{\rho}|$. We have found that satisfactory results are achieved within 10 iterations ($t \leq 10$).

3) Solving x^{k+1} in v^{k+1}: We define $\lambda_2 = \beta/\rho$, $0 < q \leq 1$.

$$x^{k+1} = \arg\min_{x} \beta||x||_q^q + (z_2^k)^T(u^{k+1} - \mathcal{C}x)$$
$$+ \frac{\rho}{2}||u^{k+1} - \mathcal{C}x||_2^2,$$
$$= \arg\min_{x} \lambda_2||x||_q^q + \frac{1}{2}||u^{k+1} - \mathcal{C}x + \frac{z_2^k}{\rho}||_2^2. \quad (17)$$

If $q = 1$, this problem is ℓ_1-regularized and the ADMM generally solves it using Lasso (least absolute shrinkage and selection operator) [23]. However, factorizing $\mathcal{C}$ or computing $\mathcal{C}^T\mathcal{C}$ is not straightforward because it involves explicitly forming the matrix version of $\mathcal{C}$. Therefore we employ the $\mathcal{R}$ and $\mathcal{C}$

transforms through a filtered back projection and Fourier transform [41]. The problem in (17) is consequently solved using two-step iterative shrinkage/thresholding (TwIST) [42]. This method offers fast convergence rate for ill-conditioned problems (the condition number of $\mathcal{C}$ increases as the number of projections decreases. An analysis of the ill-conditioned nature of $\mathcal{C}$ can be found in [30]). Starting with $\check{x}^0 = x^k$, the iterative process proceeds as follows.

$$d = \check{x}^t + \mathcal{R}\left(u^{k+1} - \mathcal{C}\check{x}^t + \frac{z_2^k}{\rho}\right), \quad (18a)$$

$$\check{x}^{t+1} = (1 - \varrho)\check{x}^{t-1} - \varrho\check{x}^t + 2\varrho\mathcal{S}_{\lambda_2}(d), \quad (18b)$$

$$\mathcal{S}_{\lambda_2}(d) = \frac{\max(|d| - \lambda_2, 0)}{(\max(|d| - \lambda_2, 0) + \lambda_2)}d, \quad (18c)$$

where ϱ is a two-step parameter, defined as in [42], t is an internal iteration counter, and $\mathcal{S}_\tau(\bullet)$ is a soft-shrinkage operator with a threshold $\lambda_2 > 0$. The iteration process stops when $||\check{x}^{t+1} - \check{x}^t||/||\check{x}^t|| < \epsilon$, $x^{k+1} = \check{x}^{t_{final}}$.

If $0 < q < 1$, we employ the TwIST method with the GST defined in (16b)-(16d). Also, we include a gradient descent step size $\frac{v}{t} > 0$, where t is an internal iteration counter. This leads to convergence for non-convex problems [43]. Consequently, the gradient addition step in (18a) and the shrinkage/thresholding in (18c) become (19a) and (19b), respectively.

$$d = \check{x}^t + \frac{v}{t}\mathcal{R}\left(u^{k+1} - \mathcal{C}\check{x}^t + \frac{z_2^k}{\rho}\right), \quad (19a)$$

$$\mathcal{S}_{\lambda_2}(d) = \frac{|T_q^{GST}(d, \lambda_2)|}{(|T_q^{GST}(d, \lambda_2)| + \tau_q(\lambda_2))}d. \quad (19b)$$

4) Computing z^{k+1}: The last step in each iteration is for updating z, which is

$$z_1^{k+1} = z_1^k + \rho\,(u^{k+1} - w^{k+1}), \quad (20a)$$
$$z_2^{k+1} = z_2^k + \rho\,(u^{k+1} - \mathcal{C}x^{k+1}). \quad (20b)$$

IV. ENHANCED LINE RESTORATION WITH EMBEDDED DEBLURRING

The lines in ultrasound images can appear blurred because of low resolution, low frequency ultrasound or motion during image acquisition. To enhance line detection performance and the visualisation of restored lines, we include an additional convolution factor in the Radon transform domain with an unknown blurring kernel D. This has the effect of further sharpening detected lines. The line model is hence modified to

$$y = \mathcal{HCD}x' + n. \quad (21)$$

The estimated x' in (21) is expected to be sharper than x in (4) leading to better accuracy of automatic line detection. The complete deconvolution problem becomes (22), where $J(\bullet)$ and $G(\bullet)$ are smoothness prior terms.

$$\hat{x}' = \arg\min_{x'}\{||y - \mathcal{HCD}x'||_2^2 + \alpha'||\mathcal{CD}x'||_p^p$$
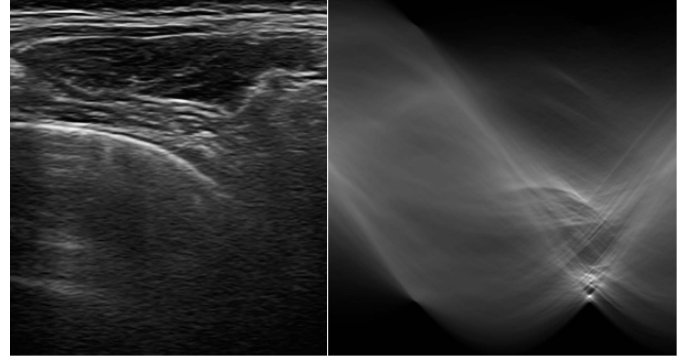$$+ \beta'||\mathcal{D}x'||_q^q + \mu'_1\,J(x') + \mu'_2\,G(\mathcal{D})\}. \quad (22)$$

Fig. 2. Example of lung ultrasound image y (Left column) and its Radon transform $R(y)$ (Right column), where the horizontal axis is θ varying from $-45°$ to $135°$, the vertical axis is r varying from $-r_{max}$ to r_{max}, and the brighter intensity indicates higher magnitude of the Radon transform.

Using the ADMM approach, we then have

$$f(u) = ||y - \mathcal{H}u||_2^2, \quad u = w = \mathcal{C}x = \mathcal{CD}x', \quad (23a)$$
$$g(v) = \alpha'||w||_p^p + \beta'||x||_q^q + \mu'_1\,J(x') + \mu'_2\,G(\mathcal{D}), \quad (23b)$$

$$v' = \begin{bmatrix} w \\ x \\ x' \end{bmatrix}, \quad \mathcal{A}' = \begin{bmatrix} \mathcal{I} \\ \mathcal{I} \\ \mathcal{I} \end{bmatrix}, \quad \mathcal{B}' = \begin{bmatrix} \mathcal{I} & 0 & 0 \\ 0 & \mathcal{C} & 0 \\ 0 & 0 & \mathcal{CD} \end{bmatrix}. \quad (23c)$$

The Lagrange multiplier becomes $z = [z_1\,z_2\,z_3]^T$. We solve u, w and x similarly to the implementation described in Section III-B and x' is computed using (24), where $\lambda_3 = \mu'_1/\rho$, $\lambda_4 = \mu'_2/\rho$ and $\vartheta = u^{k+1} + z_3^k/\rho$.

$$x'^{k+1} = \arg\min_{x'}\;\lambda_3\,J(x') + \lambda_4\,G(D) + \frac{1}{2}||\vartheta - \mathcal{CD}x'||_2^2. \quad (24)$$

The sharpened Radon transform domain x' is solved using blind deconvolution because D is unknown. In addition, D is spatially variant, so we process the areas around the local peaks $\{P_L, \Theta_L\}$ separately and merge them with a Gaussian weight. We employ a total variation blind deconvolution [44] to produce the results in this paper. We investigated several blind deblurring techniques and found each with slightly different results. We define a rectangular patch (we use the size of 300×300 pixels in this paper), ω_D is a Gaussian weight with $\sigma = 1$ and η is a normalisation term, then the result of a blind deconvolution of each patch $\tilde{x}'$ is combined as

$$x'^{k+1} = \frac{1}{\eta}\sum_{\forall\{r,\theta\}\in\{P_L,\Theta_L\}}\omega_D\tilde{x}'_{\{r,\theta\}}. \quad (25)$$

V. AUTOMATIC B-LINE DETECTION IN LUNG ULTRASOUND IMAGES

This section presents the proposed scheme for identifying the pleural line, A-lines, B-lines and Z-lines in the Radon transform domain after all lines have been detected. The scheme firstly detects the pleural line in order to locate the lung space where line artefacts occur. Then, the local peaks of the Radon transform are detected and line-type classification is done following clinical definitions, in the spatial image domain. A block diagram of the proposed automatic
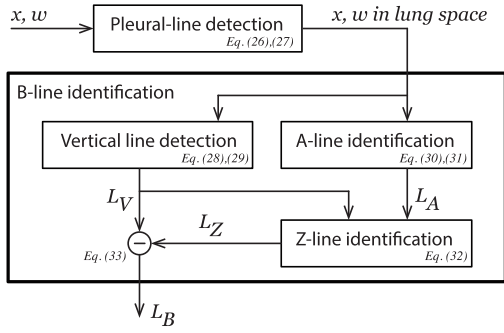
Fig. 3.   Block diagram of the proposed automatic B-line detection method.
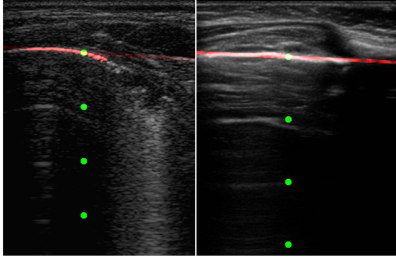

Fig. 4.   Detected Pleural line (Red) with its estimated location L_p (straight line) and the estimated positions of the A-lines (Green).

B-line detection method is shown in Fig. 3, including relevant equations used at each step.

A. Pleural-Line Detection

The pleural line normally appears to be very bright, but it is not always the brightest line in the image. This depends on the ultrasound machine settings and the position of the probe: when the chest wall and intercostal muscles may be clearly visible as shown in Fig. 4 (right), this leads to incorrect detection of the pleural line if the brightest line is used. The pleural line is the border of lung parenchyma area, which appears darker than the pleural line. We can consequently exploit this as a constraint to detect the pleural line and limit Θ_P to $\Theta_P \in \{90° \pm 20°\}$ as it is always nearly horizontal.

To reduce the probability of misdetection of the pleural line, the brightness of the area above the pleural line should be dimmed. We therefore apply a weight ω_p to the Radon representation x, as follows. Firstly, the areas in x with possible strong lines are marked using a threshold τ_p, creating $B_p = 1$ where $x > \tau_p$. τ_p is defined following the observation that the length of the pleural line is longer than half the width of the ultrasound image, as in some cases the rib is present in the image (Fig. 1 left and right), resulting in the pleural line not showing across the width of the image (cf Fig. 1 middle). Also, the intensity is always larger than 0.75 (the intensity of the ultrasound image is scaled from 0 to 1), so $\tau_p = 0.5 \times 0.75 = 0.375$. Then, the smallest radius r_τ on B_p is used as a boundary to apply the weight $\omega_p(r)$ to each r of x, according to

$$\omega_p(r) = \begin{cases} (r - r_{max})/(r_\tau - r_{max}) & \text{if } r > r_\tau \\ 1 & \text{if } r \leq r_\tau, \end{cases} \quad (26)$$

where r_{max} is the maximum radius, $r_{max} = \frac{1}{2}\sqrt{h^2 + w^2}$. The values of the area beyond r_τ is suppressed by the weight $w_p(r)$. Consequently, the pleural line location L_p is selected from the point (r_p, θ_p) that has the largest value of $\omega_p(r)x(r, \theta), r \in (-r_{max}, r_{max}], \theta \in \Theta_p$, which is

$$\{r_p, \theta_p\} = \arg\max_{r, \theta} \omega_p(r)x(r, \theta), \quad (27a)$$

$$L_p = \mathcal{C}x(r_p, \theta_p). \quad (27b)$$

Note that with $\tau_p = 0.375$, the proposed scheme achieves 96% accuracy in detecting the pleural lines in 100 test lung ultrasound images acquired with various scanners and settings as detailed in Section VI-B.

B. B-Line Identification

1) Vertical Line Detection: The procedure for B-line identification starts with detecting the vertical lines in the image by limiting $\Theta_V \in \{\pm 20°\}$. These detected vertical lines can be either B-lines or Z-lines. Therefore, the B-line definitions are applied in order to distinguish between them. The constraints of the B-lines are i) not being erased by the A-lines, and ii) having long length. Although the definition of B-lines states that the comet artefacts continue to the bottom of the ultrasound image, for in vivo ultrasound images, this condition might not be always true because of amplitude attenuation, which is not compensated perfectly. According to these constraints, we create a binary mask ω_B using a threshold τ_B, which allows the line brightness in the image domain to attenuate approximately linearly from 1 at the pleural line to 0 at the bottom of the image (the distance between the pleural line and the bottom of the image is h_{lung}). That means, $\tau_B = h_{lung}/2$ and

$$\omega_B(r, \theta) = \begin{cases} 1 & \text{if } x(r, \theta) > \tau_B \\ 0 & \text{otherwise.} \end{cases} \quad (28)$$

This threshold is set to account for the case of low-quality image, where the brightness at the bottom of the image is lower than that at the top of the image. Then, the vertical lines L_V are detected as follows.

$$\{P_V, \Theta_V\} = \mathcal{L}(\omega_B(r, \theta)x(r, \theta), \tau_L), \ \theta \in \Theta_B, \quad (29a)$$

$$L_V = \mathcal{C}x(P_V, \Theta_V)\mathcal{C}x. \quad (29b)$$

where $\mathcal{L}(\bullet)$ is a local-maximum operator which gives a list of positions $\{X, Y\}$ where local peaks occur within the radius τ_L. P_V and Θ_V are a list of r and a list of θ, respectively. We employ a grayscale dilation with a flat structuring element for the function $\mathcal{L}(\bullet)$ [45]. τ_L is defined using the smallest distance between the blobs on the pleural line, since the vertical lines originate at the pleural line.

2) A-Line Identification: The A-lines – physiological horizontal lines below the pleural line – are detected using $\Theta_A = \Theta_P$, using the fact that they are equidistant, and the distance between them is equal to the distance between skin and pleural line, denoted g_A. This distance is defined as $g_A = \bar{i}_p$, $i_p \in L_p$, where i_p is a position in the vertical axis of the image and $\bar{i}_p$ represents mean value. In Fig. 4 the green dots demonstrate the equidistant reflections at intervals equal

p		0.5			1			2	
q	0.1	0.5	1	0.1	0.5	1	0.1	0.5	1
precision	1.00±0.04	0.97±0.08	0.92±0.09	0.99±0.09	0.91±0.10	0.84±0.12	0.94±0.10	0.89±0.09	0.76±0.07
recall	0.81±0.11	0.91±0.09	0.96±0.05	0.90±0.09	0.93±0.06	0.99±0.04	0.89±0.08	0.96±0.05	1.00±0.00

*mean±standard deviation

to the gap between the top border of the image (skin) and the pleural line. These can consequently be used for limiting the possible A-line occurrences. Fig. 4 (right) also shows the echoic lines of intercostal muscles between the pleural line and the first A-line. The B-lines delete these echoic lines as well, hence we also employ them to distinguish between B-lines and Z-lines. We create a binary map of the possible areas of the A-lines ω_A, defined as

$$\omega_A(i,j) = \begin{cases} 1 & \text{if } i \in [\frac{h}{2} - g_A, \frac{h}{2} - 2\ g_A] \\ 1 & \text{if } i \in [\frac{h}{2} - kg_A - \tau_g, \frac{h}{2} - kg_A + \tau_g] \\ 0 & \text{otherwise} \end{cases} \quad (30)$$

where k is a counter, $k = \{2, 3, \ldots, \lfloor \frac{h_{lung}}{g_A} \rfloor\}$ and τ_g is half the possible A-line width (we found that τ_g=3 pixels give the best result. The variation of τ_g does not significantly affect the results as long as the thickness of the A-lines is smaller than the gap between them). Then, the A-line location L_A is computed as follows:

$$x_A = \mathcal{R}\omega_A \quad (31a)$$

$$\{P_A, \Theta_A\} = \mathcal{L}(x(r, \theta), g_A), \quad r \in x_A, \ \theta \in x_A \cap \Theta_A \quad (31b)$$

$$L_A = \mathcal{C}x(P_A, \Theta_A)\mathcal{C}x. \quad (31c)$$

3) Z-Line Identification: The A-lines are erased by the B-lines, so any vertical artefacts in the presence of the A-lines are defined as Z-lines which have no use for diagnosis. Therefore, the Z-line position L_Z can be identified as

$$L_Z = \mathcal{C}\{\mathcal{R}(L_V \cap L_A), \theta\}\mathcal{C}x, \quad \theta \in \Theta_B. \quad (32)$$

4) B-Line Identification: Finally, B-line positions L_B can be obtained by subtracting the Z-lines from the previously detected vertical lines.

$$L_B = L_V - L_Z. \quad (33)$$

VI. RESULTS AND DISCUSSION

A. Simulated Ultrasound Images

We tested our proposed method on 50 simulated images, degraded by convolution with a simulated ultrasound PSF as in [32]. Different size images were generated varying from 250×250 pixels to 600×600 pixels to induce and evaluate different characteristics in the Radon transform domain. The simulated images were first created from 6-10 lines with different thickness (1-2 0 pixels), angles (0-90 degrees) and positions (similar to lines in lung ultrasound images). Then, they were blurred using a Gaussian low-pass filter with $\sigma = 1$. Next, a random multiplicative noise was added and convolution with the simulated ultrasound PSF was performed on this speckle result. An example simulated image is shown in Fig. 5,
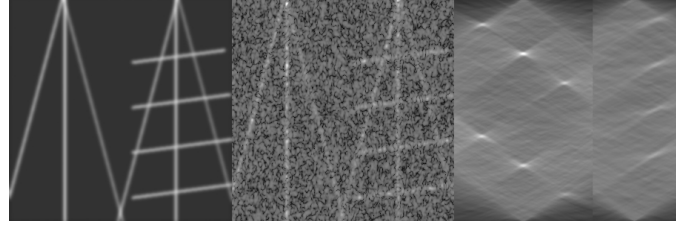

Fig. 5. Simulated ultrasound image. (Left) Line image. (Middle) B-mode image. (Right) Radon transform image with $\Theta \in \{\pm 25°, 90° \pm 15°\}$.

where the line structure, the corresponding B-mode image and its Radon transform representation are shown from left to right, respectively.

The results of line restoration for the image of Fig. 5 are shown in Fig. 6 with various values of p and q. It is obvious that small p and q remove most noise thereby producing sparser results. However, too small values may attenuate peak values in the Radon transform domain, causing some weak lines to go undetected. The precision and recall values for line detection are shown in Table I. The precision was computed from the total number of correctly detected B-lines divided by the number of all detected B-lines. The recall was computed from the total number of correctly detected B-lines divided by the total number of true B-lines. High precision means that lines are rarely misidentified, whilst high recall (or true positive rate) means most true lines are correctly identified. The best harmonic mean of precision and recall are obtained for $p = 1$ and $q = 0.1$, followed by slightly lower value at $p = 0.5$ and $q = 0.5$.

B. In Vivo Ultrasound B-Mode Images

The ultrasound images used in this work were acquired at the bedside with a commercially available portable device (SonoSite S-ICU C60; SonoSite; Bothell, WA) equipped with a 6- to 13-MHz linear probe (L25x; SonoSite) in B-mode. These images have already been used in two previous clinical studies [2], [3], were information on the patient cohort was extensively detailed. The images were acquired from 23 children aged 0.8-18 (8 patients with acute kidney injury (AKI), 15 patients with end-stage renal disease (ESRD)). Note that real ultrasound images are generally acquired with two types of transducers, either linear or convex. Convex transducers produce a wider field of view, but can make line detection more difficult. We therefore transform these curved images to rectangular ones before applying our proposed method. This can be done automatically by detecting straight side edges and applying an affine transform. The blurring kernel is unknown in the in vivo study, hence we
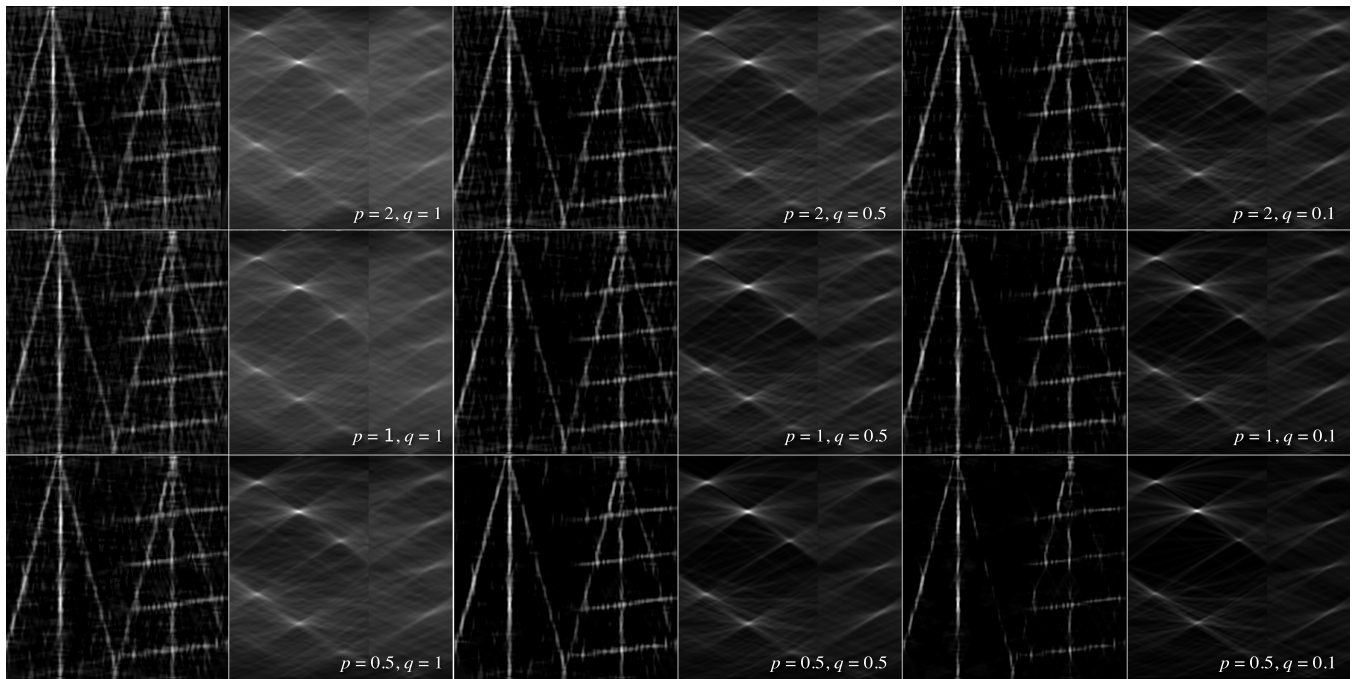
Fig. 6. Results of Cx and x ($\Theta \in \{\pm 25°, 90° \pm 15°\}$) when $p = 2$ (top row), $p = 1$ (middle row), $p = 0.5$ (bottom row), and $q = 1$ (colume 1-2), $q = 0.5$ (colume 3-4), $q = 0.1$ (colume 5-6).
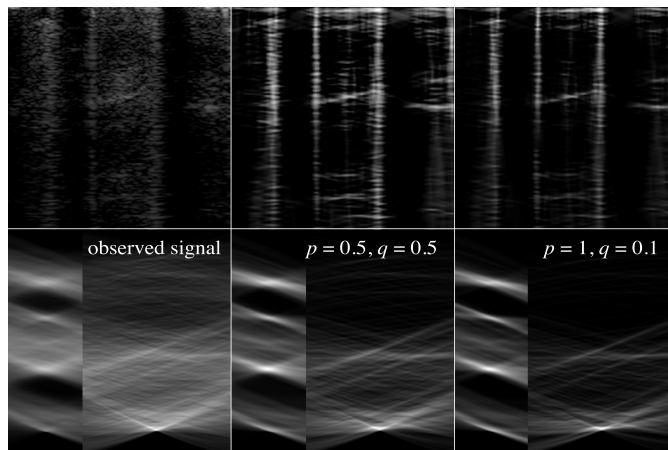

Fig. 7. Restored lines of the in vivo aerated lung ultrasound images, containing four B-lines (left), using $p = 0.5$, $q = 0.5$ (middle) and $p = 1$, $q = 0.1$ (right). (Top row) lines in B-mode images. (Bottom row) Radon transform domains.
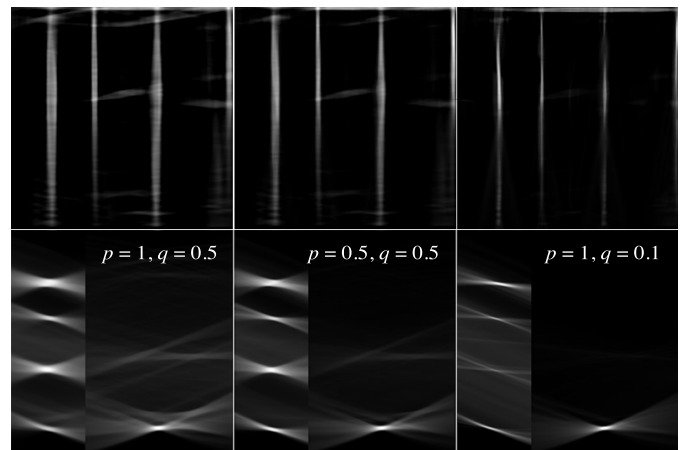

Fig. 8. Restored lines when the deblurring is included, using $p = 1$, $q = 0.5$ (left), $p = 0.5$, $q = 0.5$ (middle), and $p = 1$, $q = 0.1$ (right). (Top row) line positions. (Bottom row) deblurred Radon transform domains.

estimate it by adopting a method originally proposed in [13] for the PSF of the RF data, and applying it on our actual B-mode ultrasound images. The maximum magnitudes of the estimated blurring kernel are in the range 0-0.2 and the shape of its distribution is not isotropic. Let us note here that we simply estimate a generic blurring kernel, routinely encountered in any imaging modality and due to the limited bandwidth of imaging devices. However, our entire framework can be employed with no alterations on the RF data, in which case, the estimated blurring kernel would correspond to the PSF in the standard convolutive ultrasound image formation model. We believe this to contribute to the versatility of our proposed framework, making it applicable in general, of course

after minor adaptations, to other types of imaging modalities where line detection is necessary.

Fig. 7 and Fig. 8 show a cropped area under the pleural line of a lung ultrasound image containing four B-lines, with and without the enhanced method (described in Section IV), respectively. Five and four vertical lines were detected in Fig. 7 and Fig. 8, respectively. Four of these vertical lines were correctly identified as B-lines. One vertical line in Fig. 7 was discounted because of the detected A-line. The results of the deblurring enhancement obviously shows better line structures, but all textures, which might be useful for clinical assessment, are also removed.

We investigated image enhancement performance, which was the by-product of the deconvolution process, using a
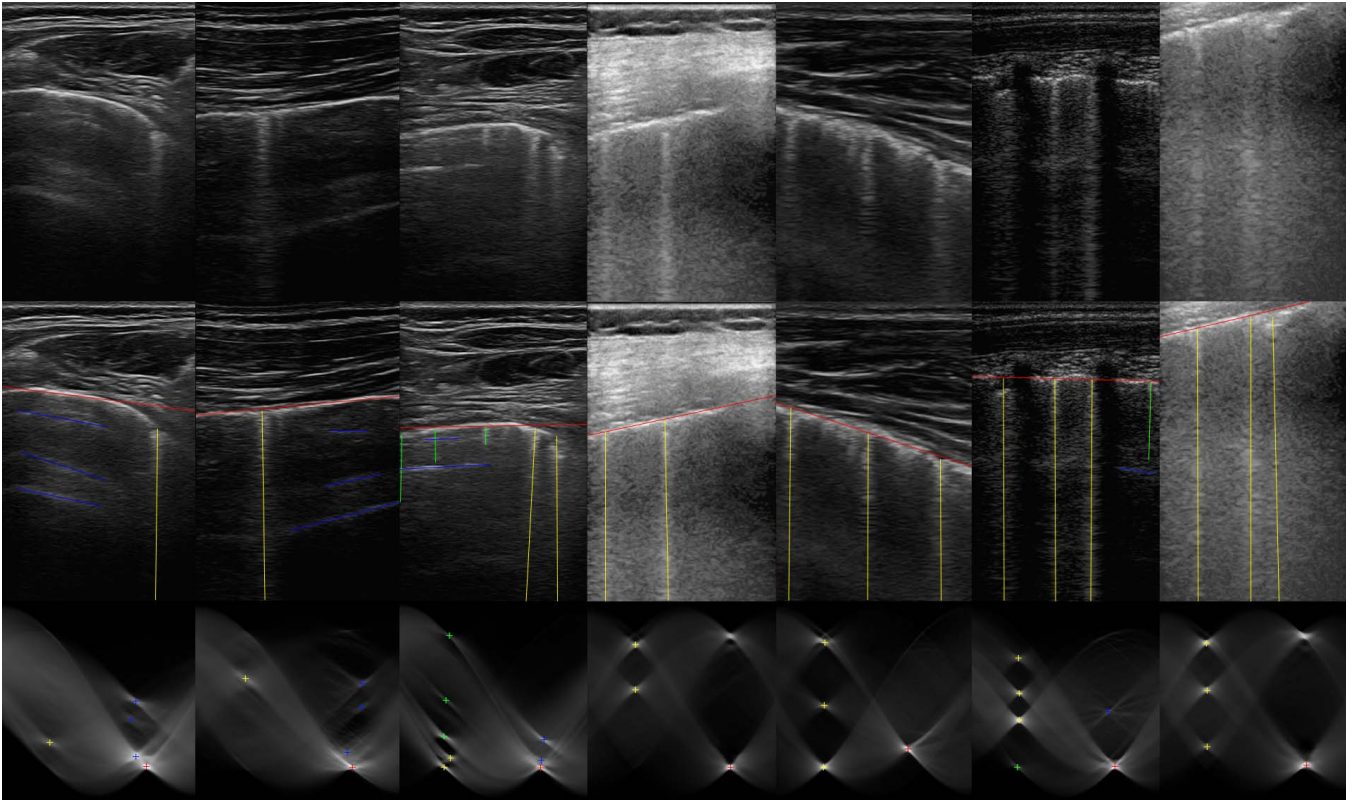
Fig. 9. Original B-mode ultrasound image (top row), detected lines (middle row) and Radon transform domain representation of the restored B-mode images using $p = q = 0.5$ (bottom row). Red, yellow, blue and green lines represent the pleural lines, B-lines, A-lines and Z-lines, respectively.

TABLE II
CNR ASSESSMENT FOR IN VIVO DATA*

original	STICKS [17]	HOUGH [21]	AWBF [14]	proposed p=0.5, q=0.5 w/o $\mathcal{D}$	w $\mathcal{D}$
1.16±0.51	1.37±0.48	1.42±0.22	1.40±0.32	2.33±0.20	2.47±0.15

*mean±standard deviation

contrast-to-noise ratio (CNR) as the true tissue reflectivity function is unknown. The CNR is defined as $(|\mu_1 - \mu_2|)/\sqrt{\sigma_1^2 + \sigma_2^2}$, where μ_1 and μ_2 are the mean of pixels located in two regions, while σ_1^2 and σ_2^2 are the variances of these two regions [46]. We selected the first region as the area where the lines were and the second region as the area around the first region. We compared our proposed method with three existing techniques: i) line detection using eight sticks as a rotating kernel transformation (STICKS) [17], ii) line detection with log regularised Hough transform (HOUGH) [21], and iii) despeckling approach with AWBF [14] followed by Radon transform. The results of the average of 100 B-mode ultrasound images are shown in Table II. The proposed method with deblurring achieves the best CNR and outperforms the existing methods by up to approximately 80%.

C. B-Line Identification

We tested our proposed automatic B-line detection method (described in Section V-B) on 100 in vivo ultrasound B-mode images of children. The lines in each

image were restored using the method described in Section III and Section IV and HOUGH [21]. We also applied our B-line identification method to the results of STICKS [17] and AWBF [14]. We evaluated these techniques using as ground truth lines identified visually by clinical experts.

We compared our method with two existing approaches for automatic B-line detection, which are i) summation of angular features and thresholding (AFT) [8] and ii) alternate sequential filtering and iterative morphological process (ASF) [9]. Table III shows the B-line detection performance measured using F_β score, where β is a weight. The F-score measures the accuracy of binary data retrieval by considering the precision and the recall:

$$F_\beta = (1 + \beta^2) \frac{\text{precision} \cdot \text{recall}}{\beta^2 \text{precision} + \text{recall}}. \quad (34)$$

The balanced F_1-score is the harmonic mean of precision and recall. We also included the $F_{0.5}$-score and F_2-score to demonstrate the performance when the precision was weighted higher than the recall, and vice versa, respectively. When the precision and the recall were weighted equally, our method with the restored lines using $p = q = 0.5$ gave the best result, achieving up to 35% improvement over the existing methods.

When the precision was weighted higher than the recall – ensuring that the detected B-lines were actually the true B-lines, our method applied to our enhanced line restorations (with $\mathcal{D}$) using $p = q = 0.5$ and using $p = 1$,

TABLE III
B-LINE IDENTIFICATION PERFORMANCE*

score	method	STICK [17]	HOUGH [21]	AWBF [14]	proposed $p=2$, $q=1$		proposed $p=1$, $q=1$		proposed $p=0.5$, $q=0.5$		proposed $p=1$, $q=0.1$	
					w/o $\mathcal{D}$	w $\mathcal{D}$	w/o $\mathcal{D}$	w $\mathcal{D}$	w/o $\mathcal{D}$	w $\mathcal{D}$	w/o $\mathcal{D}$	w $\mathcal{D}$
$F_{0.5}$	AFT [8]	0.63±0.22	0.64±0.24	0.64±0.21	0.64±0.22	0.67±0.22	0.66±0.20	0.71±0.21	0.73±0.19	0.81±0.22	0.75±0.20	0.82±0.19
	ASF [9]	0.66±0.25	0.62±0.19	0.65±0.24	0.67±0.21	0.68±0.21	0.70±0.20	0.69±0.23	0.70±0.22	0.87±0.18	0.70±0.20	0.87±0.19
	proposed	0.68±0.23	0.74±0.20	0.71±0.22	0.74±0.19	0.85±0.19	0.78±0.18	0.87±0.19	0.93±0.16	**0.97±0.15**	0.89±0.19	**0.97±0.16**
F_1	AFT [8]	0.69±0.23	0.68±0.23	0.69±0.27	0.71±0.22	0.74±0.20	0.73±0.21	0.77±0.19	0.77±0.22	0.76±0.20	0.78±0.21	0.74±0.21
	ASF [9]	0.72±0.28	0.67±0.23	0.69±0.24	0.73±0.20	0.74±0.21	0.75±0.19	0.75±0.21	0.75±0.20	0.79±0.21	0.74±0.21	0.81±0.18
	proposed	0.74±0.21	0.73±0.20	0.74±0.28	0.80±0.19	0.88±0.17	0.83±0.18	0.89±0.17	**0.94±0.17**	0.94±0.18	0.91±0.19	0.92±0.17
F_2	AFT [8]	0.77±0.27	0.72±0.24	0.74±0.29	0.80±0.22	0.83±0.21	0.82±0.20	0.84±0.18	0.82±0.20	0.71±0.22	0.80±0.22	0.67±0.26
	ASF [9]	0.81±0.25	0.73±0.20	0.77±0.24	0.81±0.20	0.83±0.23	0.80±0.19	0.81±0.18	0.81±0.19	0.72±0.21	0.78±0.19	0.75±0.20
	proposed	0.81±0.25	0.75±0.20	0.78±0.23	0.88±0.20	0.92±0.17	0.88±0.19	0.91±0.17	**0.96±0.14**	0.90±0.16	**0.93±0.18**	0.88±0.19

*mean±standard deviation

$q = 0.1$ outperform the others by up to 50%. The AFT and ASF approaches overestimate the number of B-lines when it is between 0-3, since A-lines are not taken into account, resulting in Z-lines being misclassified. When the recall was weighted higher than the precision – ensuring that all B-lines are detected, our method (applied to our enhanced line restoration methods (without $\mathcal{D}$)) using $p = q = 0.5$ and using $p = 1$, $q = 0.1$ outperforms the others by up to 33%. AFT and ASF underestimate when the number of B-lines is more than 2, since the shadow of the ribs in children cause unclear/fade laser-like artefacts, unlike those in the adult cases.

The results in Table III reveal that the enhanced line restoration improves B-line identification performance by up to 14% when convex optimisation approaches are employed ($p \geq 1$ and $q \geq 1$). The enhanced method however improves only the $F_{0.5}$-score results when non-convex optimisation approaches are used. This is because when p and q are very small, applying deblurring ($\mathcal{D}$) could decrease the amplitudes of the weak lines in the Radon transform domain and causes false negatives. Table III also shows that when testing the B-line detection with the enhanced lines in the ultrasound images by STICK, HOUGH and AWBF, our B-line detection methods also outperform the AFT and ASF techniques. This confirms the robustness of our approach.

Fig. 9 shows the line detection results for different ultrasound settings, i.e. different frequencies, different acquisition modes and different time-gain compensations. The detected pleural lines (red), A-lines (blue), B-lines (yellow) and Z-lines (green) were drawn on the original speckle ultrasound B-mode images. The second row of the figure shows the restored lines x' using $p = q = 0.5$ with deblurring $\mathcal{D}$. For the images with high levels of speckle, the detection approach can possibly give incorrect results if all local-maximum points are included without clinical insight. For example, the fourth and seventh images in Fig. 9 exhibit high noise around the bottom of the images resulting in high values of the Radon transforms indicating the presence of horizontal lines. However, the locations of these horizontal lines do not correspond to those of the possible A-lines, so they are discounted. This is a further reason why our automatic B-line detection approach performs better than the state of the art methods.

In Fig. 10, we show a receiver operating characteristic curve (ROC curve), which illustrates the performances of the B-line identification methods via true positive rates (TPR) and false positive rates (FPR) by varying thresholds.
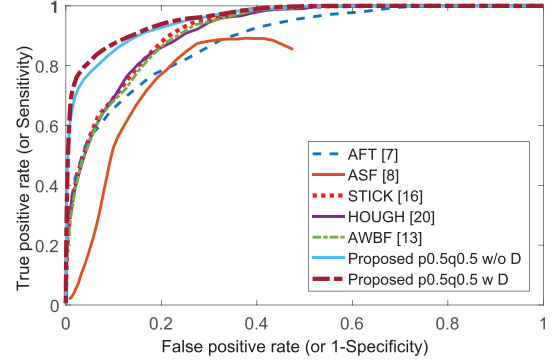

Fig. 10. Performance comparison of the B-line identification methods through a receiver operating characteristic curve (ROC curve).

TABLE IV
PARAMETERS USED IN THE PROPOSED LINE RESTORATION AND B-LINE IDENTIFICATION

parameter	process	value
p	norm for solving w	0.1-1.0 (best at 0.5)
q	norm for solving x	0.1-1.0 (best at 0.5)
ρ	penalty for ADMM	1
α	regularisation term for solving w	$0.001 \max(|y|)$
λ_1	$= \alpha/\rho$	$0.001 \max(|y|)$
β	regularisation term for solving x	$0.01 \max(|y|)$
λ_2	$= \beta/\rho$	$0.01 \max(|y|)$
ϱ	TwIST	1.96 (as used in [42])
ν	non-convex TwiST	$q/4$
μ_1	regularisation term for deblurring	$0.1 \max(|x^k|)$
μ_2	regularisation term for deblurring	$0.1 \max(|x^k|)$
ϵ	stopping criteria for iterations	10^{-3}
τ_p	pleural line detection	0.375
τ_L	vertical line detection	smallest distance between blobs
τ_g	A-line identification	3

We considered the existence of B-lines and the non-existence of B-lines as positive and negative classes, respectively. For our B-line identification method, we varied τ_B in (28) and τ_L in (29) to plot the ROC curves of STICK, HOUGH, AWBF, and our proposed line restoration with $p = q = 0.5$. For creating the ROC curves of AFT and AFS, the thresholds used with angular features and for creating a binary mask were varied, respectively. The ROC curve shows that our proposed method significantly outperforms existing ones, particular the AFS, where the binary mask cannot be used to discriminate B-lines when the threshold is too low. This also confirms that the proposed method is robust, because it achieves high sensitivity regardless of values of the thresholds.

For reproducibility of results, Table IV shows all parameters and their corresponding values as used in our implementation.

Note that increasing the values of α, β, μ_1 and μ_2 will speed up the iterative process, but the results might not be optimal because of large step size. We fixed the value of ρ to 1, which gave good results as shown in Section VI. However, ρ can be set adaptively for each iteration to improve the convergence and to reduce the effect of the initialisation on overall performance [23]. With the parameters in Table IV, using MATLAB R2016a with 64-bit OS i7-3770S CPU the computational times per image are approximately 45 and 0.75 seconds for the line restoration and subsequent B-line identification processes, respectively. This is faster than when performed by clinical experts, which generally take 3-10 min, depending on age and compliance of the patient.

VII. CONCLUSIONS

Currently, B-line identification requires specific training and it is operator dependent. Automating the detection of B-lines would widen the application of lung ultrasound and benefit dialysis nurses, patients and their families. Improving the accessibility of the technique will broaden its accessibility, with anticipated clinical benefits in improved fluid management for both children and adults on dialysis.

This paper presents a novel line detection procedure for speckle images. Lines are restored by solving an inverse problem consisting of joint deconvolution and line detection. The problem is solved based on ℓ_p regularisation and Radon transform. The method offers a simple and fast implementation via the alternating direction method of multipliers (ADMM) which divides a large problem into a series of subproblems. We offer solutions for both convex and non-convex problems. Additionally, we include a blind deconvolution step in the Radon transform domain to enhance visualisation and improve line detection performance, particularly when convex optimisation techniques are employed to restore lines.

Based on accurate line detection results, we are able to identify B-lines in lung ultrasound images automatically. This is achieved using local maxima in the Radon transform domain with additional constraints based on clinical definitions. Subjective results show accurately restored lines and objective results demonstrate that the proposed method outperforms existing approaches for B-line detection in lung ultrasound images by up to 50%. With very little adaptation, the techniques described in this work could be applied to other ultrasound applications, as well as to other medical imaging modalities where line detection can help diagnosis.

ACKNOWLEDGMENT

REFERENCES

[1] D. A. Lichtenstein, G. A. Mezière, J.-F. Lagoueyte, P. Biderman, I. Goldstein, and A. Gepner, "A-lines and B-lines: Lung ultrasound as a bedside tool for predicting pulmonary artery occlusion pressure in the critically ill," *Chest*, vol. 136, no. 4, pp. 1014–1020, 2009.

[2] M. Allinovi, M. Saleem, O. Burgess, C. Armstrong, and W. Hayes, "Finding covert fluid: Methods for detecting volume overload in children on dialysis," *Pediatr Nephrol.*, vol. 31, no. 12, pp. 2327–2335, 2016.

[3] M. Allinovi, M. Saleem, P. Romagnani, P. Nazerian, and W. Hayes, "Lung ultrasound: A novel technique for detecting fluid overload in children on dialysis," *Nephrol. Dialysis Transplantation*, vol. 32, no. 3, pp. 541–547, 2017.

[4] P. D. Nicolò, G. Magnoni, and A. Granata, "Lung ultrasound in hemodialysis: A card to be played?" *Blood Purif*, vol. 44, no. 1, pp. 1–7, 2017.

[5] C. Zoccali *et al.*, "Pulmonary congestion predicts cardiac events and mortality in ESRD," *J. Amer. Soc. Nephrol.*, vol. 24, no. 4, pp. 639–646, 2013.

[6] D. Siriopol *et al.*, "Predicting mortality in haemodialysis patients: A comparison between lung ultrasonography, bioimpedance data and echocardiography parameters," *Nephrol. Dialysis Transplantation*, vol. 28, no. 11, pp. 2851–2859, 2013.

[7] L. Gargani *et al.*, "Efficacy of a remote Web-based lung ultrasound training for nephrologists and cardiologists: A LUST trial sub-project," *Nephrol. Dialysis Transplantation*, vol. 31, no. 12, pp. 1982–1988, 2016.

[8] L. J. Brattain, B. A. Telfer, A. S. Liteplo, and V. E. Noble, "Automated B-line scoring on thoracic sonography," *J. Ultrasound Med.*, vol. 32, no. 12, pp. 2185–2190, Dec. 2013.

[9] R. Moshavegh *et al.*, "Novel automatic detection of pleura and B-lines (comet-tail artifacts) on *in vivo* lung ultrasound scans," *Proc. SPIE*, vol. 9790, pp. 1–7, Apr. 2016.

[10] W. F. Weitzel *et al.*, "Quantitative lung ultrasound comet measurement: Method and initial clinical results," *Blood Purif*, vol. 39, pp. 37–44, Jan. 2015.

[11] R. O. Duda and R. E. Hart, "Use of the hough transformation to detect lines and curves in pictures," *Commun. ACM*, vol. 15, no. 1, pp. 11–15, Jan. 1972.

[12] A. Achim, A. Bezerianos, and P. Tsakalides, "Novel Bayesian multiscale method for speckle removal in medical ultrasound images," *IEEE Trans. Med. Imag.*, vol. 20, no. 8, pp. 772–783, Aug. 2001.

[13] O. V. Michailovich and A. Tannenbaum, "Despeckling of medical ultrasound images," *IEEE Trans. Ultrason., Ferroelect., Freq. Control*, vol. 53, no. 1, pp. 64–78, Jan. 2006.

[14] N. Anantrasirichai *et al.*, "Adaptive-weighted bilateral filtering and other pre-processing techniques for optical coherence tomography," *Computerized Med. Imag. Graph.*, vol. 38, no. 6, pp. 526–539, Sep. 2014.

[15] J.-W. Lee and I.-S. Kweon, "Extraction of line features in a noisy image," *Pattern Recognit.*, vol. 30, pp. 1651–1660, 1997.

[16] W. Gao, X. Zhang, L. Yang, and H. Liu, "An improved sobel edge detection," in *Proc. IEEE Int. Conf. Comput. Sci. Inf. Technol.*, vol. 5, Jul. 2010, pp. 67–71.

[17] R. N. Czerwinski, D. L. Jones, and W. D. O'Brien, "Detection of lines and boundaries in speckle images-application to medical ultrasound," *IEEE Trans. Med. Imag.*, vol. 18, no. 2, pp. 126–136, Feb. 1999.

[18] G. Papari and N. Petkov, "Edge and line oriented contour detection: State of the art," *Image Vis. Comput.*, vol. 29, nos. 2–3, pp. 79–103, 2011.

[19] E. Magli, L. Lo Presti, and G. Olmo, "A pattern detection and compression algorithm based on the joint wavelet and Radon transform," in *Proc. 13th Int. Conf. Digit. Signal Process. (DSP)*, vol. 2. Jul. 1997, pp. 559–562.

[20] S. R. Deans, "Hough transform from the Radon transform," *IEEE Trans. Pattern Anal. Mach. Intell.*, vol. 3, no. 2, pp. 185–188, Mar. 1981.

[21] N. Aggarwal and W. C. Karl, "Line detection in images through regularized hough transform," *IEEE Trans. Image Process.*, vol. 15, no. 3, pp. 582–591, Mar. 2006.

[22] N. Anantrasirichai, M. Allinovi, W. Hayes, and A. Achim, "Automatic B-line detection in paediatric lung ultrasound," in *Proc. IEEE Int. Ultrason. Symp.*, Sep. 2016, pp. 1–4.

[23] S. Boyd, N. Parikh, E. Chu, B. Peleato, and J. Eckstein, "Distributed optimization and statistical learning via the alternating direction method of multipliers," *Found. Trends Mach. Learn.*, vol. 3, no. 1, pp. 1–122, 2011.

[24] R. Sherman, "Crackles and comets: Lung ultrasound to detect pulmonary congestion in patients on dialysis is coming of age," *Clin. J. Amer. Soc. Nephrol.*, vol. 11, no. 11, pp. 1924–1926, Sep. 2016.

[25] Z. Jambrik *et al.*, "Usefulness of ultrasound lung comets as a nonradiologic sign of extravascular lung water," *Amer. J. Cardiol.*, vol. 93, no. 10, pp. 1265–1270, May 2006.

[26] F. Mallamaci *et al.*, "Detection of pulmonary congestion by chest ultrasound in dialysis patients," *JACC, Cardiovascular Imag.*, vol. 3, no. 6, pp. 586–594, Jun. 2010.

[27] L. Gargani and G. Volpicelli, "How I do it: Lung ultrasound," *Cardiovascular Ultrasound*, vol. 12, no. 25, p. 25, 2014.

[28] M. Trezzi *et al.*, "Lung ultrasonography for the assessment of rapid extravascular water variation: Evidence from hemodialysis patients," *Internal Emergency Med.*, vol. 8, no. 5, pp. 409–415, 2013.

[29] A. Kak and M. Slaney, *Principles of Computerized Tomographic Imaging*. New York, NY, USA: IEEE Press, 1988.

[30] B. T. Kelley and V. K. Madisetti, "The fast discrete Radon transform. I. Theory," *IEEE Trans. Image Process.*, vol. 2, no. 3, pp. 382–400, Jul. 1993.

[31] MathWorks. *Radon Transform*, accessed on Jan. 8, 2017. [Online]. Available: http://mathworks.com/help/images/ref/radon.html

[32] Z. Chen, A. Basarab, and D. Kouamé, "Compressive deconvolution in medical ultrasound imaging," *IEEE Trans. Med. Imag.*, vol. 35, no. 3, pp. 728–737, Mar. 2016.

[33] O. V. Michailovich and D. Adam, "A novel approach to the 2-D blind deconvolution problem in medical ultrasound," *IEEE Trans. Med. Imag.*, vol. 24, no. 1, pp. 86–104, Jan. 2005.

[34] N. Anantrasirichai, J. Burn, and D. R. Bull, "Projective image restoration using sparsity regularization," in *Proc. 20th IEEE Int. Conf. Image Process. (ICIP)*, Sep. 2013, pp. 1080–1084.

[35] A. Zanforlin *et al.*, "B-lines: To count or not to count?" *JACC, Cardiovascular Imag.*, vol. 7, no. 6, pp. 635–636, Jun. 2014.

[36] A. Achim, B. Buxton, G. Tzagkarakis, and P. Tsakalides, "Compressive sensing for ultrasound RF echoes using a-stable distributions," in *Proc. Int. Conf. IEEE Eng. Med. Biol.*, Aug. 2010, pp. 4304–4307.

[37] A. Achim, A. Basarab, G. Tzagkarakis, P. Tsakalides, and D. Kouamè, "Reconstruction of ultrasound RF echoes modeled as stable random variables," *IEEE Trans. Comput. Imag.*, vol. 1, no. 2, pp. 86–95, Jun. 2015.

[38] M. Hong, Z.-Q. Luo, and M. Razaviyayn. (Oct. 2014). "Convergence analysis of alternating direction method of multipliers for a family of nonconvex problems." [online]. Available: https://arxiv.org/abs/1410.1390

[39] N. Parikh and S. Boyd, "Proximal algorithms," *Found. Trends Optim.*, vol. 1, no. 3, pp. 123–231, 2013.

[40] W. Zuo, D. Meng, L. Zhang, X. Feng, and D. Zhang, "A generalized iterated shrinkage algorithm for non-convex sparse coding," in *Proc. IEEE Int. Conf. Comput. Vis.*, Sydney, NSW, Australia, Dec. 2013, pp. 217–224.

[41] A. Brandt, J. Mann, M. Brodski, and M. Galun, "A fast and accurate multilevel inversion of the Radon transform," *SIAM J. Appl. Math.*, vol. 60, no. 2, pp. 437–462, 1999.

[42] J. M. Bioucas-Dias and M. A. T. Figueiredo, "A new TwIST: Two-step iterative shrinkage/thresholding algorithms for image restoration," *IEEE Trans. Image Process.*, vol. 16, no. 12, pp. 2992–3004, Dec. 2007.

[43] M. Chiang, "Nonconvex optimization for communication networks," *Adv. Appl. Math. Global Optim.*, vol. 17, pp. 137–196, Feb. 2009.

[44] T. F. Chan and C.-K. Wong, "Total variation blind deconvolution," *IEEE Trans. Image Process.*, vol. 7, no. 3, pp. 370–375, Mar. 1998.

[45] R. C. Gonzalez, R. E. Woods, and S. L. Eddins, *Digital Image Processing Using MATLAB*. Knoxville, USA: Gatesmark Publishing, 2009.

[46] A. Lyshchik *et al.*, "Elastic moduli of thyroid tissues under compression," *Ultrason. Imag.*, vol. 27, no. 2, pp. 101–110, 2005.